Research Square

Preprints are preliminary reports that have not undergone peer review.
They should not be considered conclusive, used to inform clinical practice,
or referenced by the media as validated information.

Biomass L-Lysine Modified PVDF-TrFE Composite Triboelectric Nanogenerator for High-Efficiency Mechanical Energy Harvesting and Self-Powered Intelligent Sensing

Wei Li

liweidting@juwp.edu.cn

Jiangxi University of Water Resources and Electric Power

Mouyue Zhu

Jiangxi University of Water Resources and Electric Power

Ziliang Xie

Jiangxi University of Water Resources and Electric Power

Hongji Guan

Jiangxi University of Water Resources and Electric Power

Qiyuan Zong

Jiangxi University of Water Resources and Electric Power

Kexin Chen

Jiangxi University of Water Resources and Electric Power

Shenyu Qiu

Jiangxi University of Water Resources and Electric Power

Xuan Peng

Jiangxi University of Water Resources and Electric Power

Wenchao Zhai

Jiangxi University of Water Resources and Electric Power

Research Article

Keywords: L-lysine, triboelectric nanogenerator, PVDF-TrFE, biomass modification, self-powered sensing

Posted Date: September 18th, 2026

DOI: https://doi.org/10.21203/rs.3.rs-11067424/v1

License: This work is licensed under a Creative Commons Attribution 4.0 International License.
Read Full License

Additional Declarations: No competing interests reported.

Abstract

Poly(vinylidene fluoride-trifluoroethylene) (PVDF-TrFE)-based triboelectric nanogenerators (TENGs) are constrained by insufficient polar functional groups and low surface charge density, limiting their efficacy in high-precision smart sensing. Conventional modification strategies largely rely on inorganic fillers or hazardous chemical additives, which undermine biocompatibility and sustainability required for next-generation green electronics. Herein, we report an eco-friendly biomass-mediated modification strategy to fabricate L-lysine-doped PVDF-TrFE composite triboelectric nanogenerators (PL-TENG). Incorporation of natural L-lysine induces hierarchical micro-nanoporous architectures, enhances interfacial polarization, and introduces efficient charge-trapping sites within the polymer matrix. At an optimal doping loading of 5 wt%, the PL-TENG delivers an open-circuit voltage of 239 V and a peak power density of 640.7 mW/m², while retaining stable electrical output over 3000 operational cycles. Leveraging its superior electromechanical sensitivity, two proof-of-concept smart-sensing applications are demonstrated. First, a microcontroller-integrated system that captures page-turning mechanical signals for real-time reading-behavior statistics. Second, a hybrid CNN-LSTM deep learning network achieving 92% classification accuracy for five hand-gripped geometric objects using single-channel triboelectric waveforms. This work presents a sustainable pathway toward high-performance TENGs, offering significant potential for self-powered sensing and artificial-intelligence-assisted human-machine interfaces.

Introduction

Driven by continuous miniaturization and widespread proliferation of distributed Internet-of-Things (IoT) electronics, sustainable micro-energy harvesting technologies are urgently required to complement or replace conventional chemical-battery power supplies (Fan et al. 2012; Zhang et al. 2018; Zhang et al. 2020; Montero et al. 2024). Triboelectric nanogenerators (TENGs), operating via the coupled effect of contact electrification and electrostatic induction, represent a promising avenue for scavenging ubiquitous ambient mechanical energy, benefiting from structural simplicity, broad material compatibility, and low fabrication cost (Nurmakanov et al. 2021; Chung et al. 2022; Xiang et al. 2024; Lee et al. 2025; Li et al. 2025; Shen et al. 2026). Beyond mechanical-energy harvesting, TENGs are widely explored as self-powered wearable sensors for human-motion monitoring and human-machine interfaces (HMI) (Troncoso et al. 2023; Ji et al. 2025; Lin et al. 2026). In line with global carbon-neutrality goals, developing high-performance TENGs constructed from environmentally benign material systems has become a critical research direction to mitigate battery-related pollution and limited service-life bottlenecks (Hasan et al. 2026; Lee 2026; Liu et al. 2026).

TENG performance critically depends on rational triboelectric-material pairing. Polyimide (PI) exhibits excellent electron-trapping capability and mechanical robustness and is frequently adopted as a negative triboelectric layer (Saadatnia et al. 2019; Fan et al. 2021). Among candidate positive triboelectric polymers, ferroelectric poly(vinylidene fluoride-co-trifluoroethylene) (PVDF-TrFE) stands out owing to favorable dielectric properties, tunable crystalline phases, and good solution-processable

flexibility (Yu et al. 2021; Kumar et al. 2024; Kumar et al. 2025). Nevertheless, pristine PVDF-TrFE suffers from limited polar functional moieties and insufficient surface-charge enrichment, restricting its practical applicability for high-precision smart-sensing scenarios (Jia et al. 2017; Jiang et al. 2020). Traditional polymer modification strategies predominantly utilize inorganic nanofillers or toxic chemical additives, which commonly incur filler agglomeration, degraded mechanical compliance, and biocompatibility risks, hindering the development of green electronic devices (Wang et al. 2021; Wibisono et al. 2025; Inbaraj et al. 2026). Therefore, exploring biomass-based modification methodologies to construct high-performance yet eco-friendly PVDF-TrFE composite triboelectric materials remains an important unmet research need (Deng et al. 2025; Deuri et al. 2025; Rana et al. 2025).

To tackle these challenges, we proposed a green biomass modification strategy utilizing naturally abundant L-lysine as a functional dopant. PVDF-TrFE composite films with gradient L-lysine doping contents were solution-cast using low-toxicity N,N-dimethylacetamide (DMAc) solvent and assembled into vertical contact- separation-mode TENGs (PL-TENG) paired with PI as the negative triboelectric counterpart (Liu et al. 2019; Meng et al. 2020). Systematic material characterizations confirm homogeneous dispersion of L-lysine within the polymer matrix, concomitant with favorable microstructural evolution and enhanced polar β-phase content (Deng et al. 2021; Hu et al. 2025). Under the optimized 5 wt% L-lysine loading, the PL-TENG delivers an open-circuit voltage of 239 V and a peak power density of 640.7 mW/m², with well-preserved output after 3000 cyclic contact-separation tests. Taking advantage of its high output and sensitive mechanical responsiveness, we further implement two smart-sensing demonstrations. A CNN-LSTM hybrid deep-learning architecture extracts spatiotemporal features from single-channel triboelectric signals generated during hand-gripping gestures, achieving 92% classification accuracy for five distinct geometric objects. Furthermore, a microcontroller-unit (MCU)-integrated self-powered reading-monitoring system is realized for real-time page-turning detection and reading-behavior logging. This work demonstrates that biomass L-lysine doping effectively improves the polarization behavior and charge-trapping efficiency of PVDF-TrFE, offering a feasible strategy for designing green polymer-based TENGs toward AI-empowered self-powered IoT sensing platforms.

Experimental section

Materials.

Poly(vinylidene fluoride-co-trifluoroethylene) (PVDF-TrFE, Mw ≈ 100,000) powders were purchased from Piezotech S.A.S (France). L-Lysine (analytical grade, purity ≥ 99%) and N,N-dimethylacetamide (DMAc, purity 99.9%, analytical grade) were obtained from Sinopharm Chemical Reagent Co., Ltd. (China). Commercial polyimide (PI, 0.1 mm), polyethylene terephthalate (PET, 0.1 mm), and carbon fiber paper (CFP) substrates were supplied by Changde BKMAM Biotechnology Co., Ltd. (China). All raw materials were used as received without further purification.

Preparation of PVDF-TrFE/L-Lysine Composite Film.

Predetermined masses of PVDF-TrFE and L-Lysine powders were dissolved in DMAc solvent. The mixture was magnetically stirred at 40°C for 6 h to produce homogeneous 6 wt% PVDF-TrFE/L-Lysine casting solution with varied L-lysine mass fractions (0, 3, 5, 7 wt%). The precursor solution was ultrasonically degassed to eliminate bubbles and improve dopant dispersion. Subsequently, the solution was blade-cast onto clean glass substrates and vacuum-dried at 60°C for 4 h to obtain freestanding PVDF-TrFE/L-lysine composite films.

Assembly of PL-TENG.

As-prepared PVDF-TrFE/L-Lysine composite film (~ 0.2 mm thickness) and commercial PI film were cut into 3 cm × 4 cm rectangular sheets, serving as positive and negative triboelectric layers, respectively. Copper conductive tape (~ 0.1 mm thick) was affixed to the rear surface of each triboelectric film as electrodes, with copper wires bonded for external electrical readout. Folded PET thin film acted as a flexible rebound spacer substrate. The composite film and PI film were adhered onto the opposing inner surfaces of the folded PET support using double-sided adhesive tape, forming a tunable air gap between the two triboelectric layers. This configuration yields a vertical contact-separation-mode PL-TENG.

Characterization and Electrical Measurements

Surface morphologies were characterized by field-emission scanning electron microscope (FESEM, Hitachi SU8020, Japan). Elemental dispersive X-ray spectroscopy (EDS) coupled with FE-SEM was used to probe elemental composition and spatial element distribution. X-ray diffraction (XRD, PANalytical X'Pert PRO, Netherlands; Cu Kα radiation, λ = 1.54184 Å, 40 kV, 15 mA) was performed over a 2θ range of 5°–90° with a step size of 0.02°. A programmable linear motor (KLDMF42-500) delivered periodic, well-defined mechanical excitation for TENG characterization. Open-circuit voltage (V_{oc}), short-circuit current (I_{sc}), and transferred charge (Q_{sc}) were measured by a Keithley 6514 programmable electrometer. Real-time data logging was implemented using a custom-built LabVIEW acquisition platform. COMSOL Multiphysics was utilized for finite-element electrostatic simulation of potential distribution within the contact-separation TENG geometry. For deep-learning classification, triboelectric time-series signals were pre-processed and fed into a CNN-LSTM hybrid network implemented in Python/TensorFlow. The MCU-based reading-timing hardware adopted analog-to-digital conversion (ADC) modules for signal acquisition and web-interface data visualization.

Results and discussion

Structural Design and Material Characterization of PL-TENG

To construct eco-friendly high-performance triboelectric devices, L-lysine-biomodified PVDF-TrFE composite films were designed as the positive triboelectric layer. Polar functional groups originating from L-lysine, combined with microstructural reconstruction, are anticipated to enhance interfacial

polarization and charge-trapping capability without elaborate post-processing treatments. The 5 wt% L-lysine-doped composite film was selected as the optimal working electrode for device assembly. The resulting PL-TENG can function as a sensitive self-powered tactile sensor. When integrated with MCU circuit, it realizes a smart reading-monitoring system: once the output voltage exceeds a preset threshold (3.6 V), the system automatically increments the recorded page count and resets the reading timer.

Figure 1 Structural design, material characterizations, and mechanical flexibility of L-lysine-modified PVDF-TrFE composite film-based TENG. **a** Schematic illustration of composite film preparation workflow. **b** SEM images of composite film surface morphology; scale bars: (I) 2 μm and (II) 20 μm. **c** XRD patterns of pristine PVDF-TrFE and L-lysine doped composite films. **d** Representative EDS spectrum of the doped composite film. **e** V_{oc} responses under finger pressing with varied contact areas. **f** Optical photographs demonstrating flat, folded, and rolled states of the composite film. **g** Comparative V_{oc} outputs for the device under flat, folded, and rolled mechanical deformation states.

Figure 1a illustrates the complete fabrication workflow for composite films and PL-TENG assembly (see Experimental Section for full procedural details). SEM observations (Fig. 1b) reveal that L-lysine incorporation generates a uniform interconnected micro-nano porous architecture assembled from densely packed micro-spherical domains. High-magnification imaging further shows abundant nano-wrinkles and nanofibrillar features homogenously embedded within the PVDF-TrFE matrix without obvious macroscopic phase separation, producing hierarchically rough surfaces. This hierarchical microstructure enlarges the effective triboelectric contact area and affords reversible elastic deformation, favoring conformal interfacial contact during repeated contact-separation cycles.

XRD analysis (Fig. 1c) demonstrates that L-lysine doping generates new diffraction peaks assigned to the (021) and (310) crystal planes, while peak intensities corresponding to ferroelectric β-phase reflections ((100)/(200), (020)/(220)) are markedly intensified with slight peak-position shifts toward higher 2θ. This phenomenon originates from hydrogen-bonding interactions between amine ($-NH_2$) groups of L-lysine and fluorine atoms along PVDF-TrFE polymer chains, inducing ordered chain rearrangement and increased polar β-phase fraction, which contributes to synergistic piezo-triboelectric performance improvement. EDS measurements (Fig. 1d) confirm homogeneous elemental distribution of C, F, plus additional O signals originating from carboxyl moieties of L-lysine, consistent with micro-structural observations. Abundant heterogeneous interfaces between L-lysine and the polymer matrix together with pore boundaries provide effective charge-trapping sites, suppressing rapid charge dissipation and neutralization and hence improving triboelectric charge density relative to neat PVDF-TrFE.

Figure 1e displays output voltage responses under multi-finger pressing conditions. Increasing the contact area by adding pressing fingers raises peak open-circuit voltage, directly reflecting contact-area modulation of triboelectric charge generation. Mechanical flexibility tests (Fig. 1f-g) confirm that after severe folding and rolling deformation, the PL-TENG still maintains high-magnitude V_{oc} output without

substantial performance decay, which is attributed to the intrinsic elasticity of the porous composite microstructure. These results verify the mechanical compliance of PL-TENG for flexible wearable-electronic scenarios.

Electrical Output Performance of PL-TENG

The electrical output of PL-TENG devices with four doping concentrations are summarized in Fig. 2a–c. The measured open-circuit voltages are 105 V(0 wt%), 203 V(3 wt%), 239 V(5 wt%), and 182 V(7 wt%), respectively. At 5wt% loading, a maximum short-circuit current of 25 μA and transferred charge of 112 nC are achieved, outperforming undoped and other doped counterparts. Excess L-lysine (7 wt%) causes performance deterioration, plausibly due to local filler aggregation that disrupts polymer-matrix continuity. Therefore, 5 wt% L-lysine is selected as the optimal doping condition for all subsequent characterizations.

Furthermore, external mechanical loading effects were systematically investigated. At fixed excitation frequency of 2 Hz, the V_{oc}, I_{sc}, and Q_{sc} increase monotonically with rising applied force (Fig. 2d–f). Under constant applied force (50 N), V_{oc} and Q_{sc} remained nearly invariant across the 1–4 Hz frequency range, whereas I_{sc} increases linearly with frequency (Fig. 2g–i). This behavior agrees with fundamental vertical contact-separation-mode TENG theory. Theoretically, V_{oc} and Q_{sc} are governed by saturated surface-charge density, which is insensitive to excitation frequency (Zhou et al. 2020). Meanwhile, I_{sc} correlates with charge-transfer rate and therefore scales positively with contact-separation cycling frequency (Sharma and Agarwal 2024).

Figure 3 Device working principle, finite-element simulation, power output characterization, and cyclic durability of PL-TENG. **a** Schematic of four sequential stages within the contact-separation working cycle: (I) pressed, (II) releasing, (III) released, and (IV) pressing. **b** COMSOL-simulated electrostatic potential distribution at increasing separation gaps (d = 0 mm to 4.6 mm). **c** Capacitor-charging curves for different capacitance loads (0.22–100 μF). **d** Load-dependent current and power-density curves. **e** Output-voltage versus external-load-resistance characteristic. **f** Circuit schematic incorporating rectifier bridge, energy-storage capacitor, and external load. **g** and **h** Magnified V_{oc} waveforms extracted from the initial and final segments of the cyclic durability test. **i** Charging curve for the storage capacitor powering a commercial thermo-hygrometer. **j** Long-term durability test over 3000 continuous contact-separation cycles.

Working Mechanism, Energy-Harvesting Capability, and Long-term Durability

Figure 3a illustrates the operating mechanism of the PL-TENG, which is based on the combined effects of contact electrification and electrostatic induction. Upon initial contact (Stage I), electron transfer occurs from PVDF-TrFE/L-Lysine composite toward PI, yielding net positive charges on the composite

film and negative surface charges on PI. As the two layers separate (Stage II), charge separation generates a potential difference and drives electron flow across the external circuit. At maximum separation (Stage III), electrostatic equilibrium is attained and external current vanishes. During re-contact (Stage IV), potential difference reverses, producing opposite-polarity current pulses. Repeating this contact-separation cycle yields alternating-current output signals.

Figure 3b presents finite-element electrostatic simulations performed using COMSOL Multiphysics, visualizing the gap-dependent potential evolution. Experimentally measured surface charge density (8.7 μC/m²) was assigned in the simulation setup. In the initial separation phase, a potential difference forms via coupling of electrostatic induction and a rapid capacitance reduction. As the gap widens and the capacitance continues to decrease, the potential is continuously amplified. At the maximum separation gap of 4.6 mm, the peak potential exceeds 239 V, and the system's electrostatic potential energy simultaneously reaches its maximum. This effectively demonstrates the conversion of mechanical energy into electrical energy and highlights the material's tremendous potential for micro-energy harvesting applications.

Energy-harvesting and impedance-matching behavior are presented in Fig. 3c-e. Capacitor-charging tests demonstrate that small-value capacitors (0.22 μF, 0.47 μF, and 2.2 μF) reach 19 V, 16.1 V, and 12 V respectively within 120 s. Under variable external-load resistance ranging from 0.1 MΩ to 1000 MΩ, output voltage increases and current decreases with rising resistance. At the matched load resistance of 20 MΩ, the PL-TENG achieves a peak instantaneous power density of 640.7 mW/m², complying with the maximum power transfer theorem. After rectification via a bridge-rectifier circuit (Fig. 3f), harvested electrical energy can be stored in capacitors to drive practical electronics. The charged storage capacitor successfully powers a commercial thermo-hygrometer (Fig. 3i); the PL-TENG also lights 324 commercial LEDs (Fig. S2c, Supporting Information). Long-term cyclic durability was assessed under fixed test conditions (50 N applied force, 2 Hz frequency, 4.6 mm gap). After 3000 consecutive contact-separation cycles, V_{oc} maintains its original amplitude without obvious degradation (Fig. 3g-j), confirming robust mechanical stability and operational reliability of the biomass-modified composite TENG.

Deep-learning-Assisted Hand-Grip Object-Recognition

Benefiting from high signal fidelity under mechanical deformation, PL-TENG transduces hand-gripping gestures into distinguishable triboelectric voltage time-series. The sensor was mounted onto five standard geometric objects: sphere, cube, cylinder, cone, and cuboid. Hand-gripping generates distinct voltage signatures (Fig. 4a), with peak output voltages of 14 V (sphere), 30 V (cube), 23 V (cylinder), 12 V (cone), and 17 V (cuboid). Signal differences arise from variance in hand-muscle distribution, contact geometry, and contact pressure distribution when grasping objects of different shapes.

A CNN-LSTM hybrid neural network was deployed for automatic waveform classification (Fig. 4b). The convolutional front-end extracts local amplitude-related spatial features from voltage waveforms; subsequent LSTM layer captures long-range temporal dependencies within sequential triboelectric

signals by coordinated operation of forget, input, and output gates inside each memory cell. By fusing spatial and temporal feature representations, the hybrid network achieves overall classification accuracy of 92% for five object classes. The corresponding confusion matrix (Fig. 4c) reveals near-perfect identification for sphere and cuboid samples. Minor misclassification events mainly occur between cone/cube and cone/cylinder categories, originating from partial similarity in grip-induced deformation patterns. These results demonstrate that single-channel triboelectric sensing combined with deep learning can realize shape-related gesture classification for self-powered HMI applications.

Self-Powered Smart Reading-Timing System

As illustrated in Fig. 5, a fully functional self-powered reading-timing system was constructed based on PL-TENG. During reading operations, page-flipping movements drive contact-separation of the PL-TENG element, producing transient voltage pulses (Fig. 5a(II)). The analog voltage signal is fed into an MCU circuit for analog-to-digital conversion; digitized data are transmitted to a laptop for real-time web-based visualization (Fig. 5b). Once the peak output voltage exceeds the predefined trigger threshold (3.6 V), the MCU executes programmed logic: incrementing page count (+ 2 pages per trigger event) and resetting the reading timer.

System validation experiments are shown in Fig. 5c Three independent page-turning triggers are captured within a 10 s measurement window. Corresponding web-interface screenshots (Fig. S3a,b, Supporting Information) show that the page-counter updates from “Current Page = 0” to “Current Page = 6”, accompanied by timer time accumulation. The complete practical demonstration is presented in Video V1 (Supporting Information). These results verify reliable mechanical-signal capture and event-triggered logic execution, proving the feasibility of PL-TENG for self-powered behavior-monitoring smart-sensing hardware.

Conclusion

In summary, we have demonstrated a green biomass-doping strategy to construct high-performance L-lysine-modified PVDF-TrFE triboelectric nanogenerators (PL-TENG). The strategic incorporation of L-lysine (optimized at 5 wt%) reconstructs the polymer matrix into hierarchically porous micro-nano architectures, and promotes the formation of polar ferroelectric β-phase via hydrogen-bonding interactions. These structural modifications introduce abundant interfacial charge-trapping sites, collectively enhancing interfacial polarization and triboelectric charge generation. Consequently, the optimized PL-TENG achieves a robust V_{oc} = 239 V and a peak power density of 640.7 mW/m^2, retaining stable performance after 3000 contact-separation cycles under 50 N applied force at 2 Hz excitation frequency. Beyond energy harvesting, the device exhibits exceptional tactile sensing capabilities, validated through two distinct paradigms: a CNN-LSTM hybrid deep learning model that analyzes single-channel triboelectric time-series waveforms to classify hand-gripped geometric objects with 92% accuracy, and an MCU-integrated, self-powered reading-timing system capable of real-time page-turning

detection and behavior logging. This work validates biomass modification as an effective, sustainable route for boosting the performance of PVDF-TrFE-based triboelectric materials, providing new design guidelines for green polymer electronics and laying the foundation for future AI-augmented, self-powered IoT sensing platforms.

Associated content

Declarations

Author information

Corresponding Author

Wei Li – School of Science, Jiangxi University of Water Resources and Electric Power, Nanchang 330099, P.R. China; Nanchang Key Laboratory of Photoelectric Conversion and Energy Storage Materials, Nanchang 330099, P.R. China; Email: liweidting@juwp.edu.cn.

Authors

Mouyue Zhu – School of Science, Jiangxi University of Water Resources and Electric Power, Nanchang 330099, P.R. China

Ziliang Xie – School of Science, Jiangxi University of Water Resources and Electric Power, Nanchang 330099, P.R. China

Qiyuan Zong – School of Science, Jiangxi University of Water Resources and Electric Power, Nanchang 330099, P.R. China

Hongji Guan – School of Science, Jiangxi University of Water Resources and Electric Power, Nanchang 330099, P.R. China

Kexin Chen – School of Science, Jiangxi University of Water Resources and Electric Power, Nanchang 330099, P.R. China

Wei Li – School of Science, Jiangxi University of Water Resources and Electric Power, Nanchang 330099, P.R. China; Nanchang Key Laboratory of Photoelectric Conversion and Energy Storage Materials, Nanchang 330099, P.R. China

Shenyu Qiu – School of Science, Jiangxi University of Water Resources and Electric Power, Nanchang 330099, P.R. China; Nanchang Key Laboratory of Photoelectric Conversion and Energy Storage Materials, Nanchang 330099, P.R. China

Xuan Peng – School of Science, Jiangxi University of Water Resources and Electric Power, Nanchang 330099, P.R. China; Nanchang Key Laboratory of Photoelectric Conversion and Energy Storage Materials,

Nanchang 330099, P.R. China;

Wenchao Zhai – School of Science, Jiangxi University of Water Resources and Electric Power, Nanchang 330099, P.R. China; Nanchang Key Laboratory of Photoelectric Conversion and Energy Storage Materials, Nanchang 330099, P.R. China;

Funding The authors acknowledge the financial support from National Natural Science Foundation of China (no. 22562017).

Notes The authors declare no competing financial interest.

Author Contributions

Mouyue Zhu: Writing—original draft, Investigation, Visualization, Data curation, Formal analysis; Ziliang Xie: Writing—original draft, Investigation, Visualization, Data curation, Formal analysis; Hongji Guan: Investigation, Visualization, Data curation; Qiyuan Zong: Investigation, Formal analysis; Kexin Chen: Investigation, Visualization; Wei Li: Conceptualization, Methodology, Writing—Review & Editing, Supervision, Project administration, Funding Acquisition; Shenyu Qiu: Conceptualization, Methodology, Writing—Review & Editing, Supervision, Funding Acquisition; Xuan Peng: Conceptualization, Methodology, Writing—Review & Editing, Funding Acquisition; Wenchao Zhai: Conceptualization, Methodology, Writing—Review & Editing, Project administration, Funding Acquisition.

References

1. Chung MH, Kim H, Yoo S, Jeong H, Yoo K (2022) Enhancement of triboelectricity based on fully organic composite films with a conducting polymer. *RSC Advances* 12(5):2820–2829. https://doi.org/10.1039/D1RA07408C
2. Deng S, Yuan J, Lin Y, Yu X, Ma D, Huang Y, Ji R, Zhang G, Yang N (2021) Electric-field-induced modulation of thermal conductivity in poly (vinylidene fluoride). *Nano Energy* 82:105749. https://doi.org/10.1016/j.nanoen.2021.105749
3. Deng X, Wu Z, Yu X (2025) Preparation and properties of triboelectric nanogenerator based on PVDF-TrFE/PMMA electrospun film. *Advanced Composites and Hybrid Materials* 8:19. https://doi.org/10.1007/s42114-024-01103-1
4. Deuri D, Mahanta J, Saikia B, Das B, Sharma B, Kim J, Gogoi P (2025) Hardwood-derived lignin as a tribo-positive filler in electrospun PVDF nanofibers for efficient triboelectric energy harvesting. *New Journal of Chemistry* 49(45):19843–19854. https://doi.org/10.1039/d5nj02897c
5. Fan F, Tian Z, Wang ZL (2012) Flexible triboelectric generator. *Nano Energy* 1(1):328–334. https://doi.org/10.1016/j.nanoen.2012.01.004
6. Fan Y, Li S, Tao X, Wang Y, Liu Z, Chen H, Wu Z, Zhang J, Ren F, Chen X, Fu E (2021) Negative triboelectric polymers with ultrahigh charge density induced by ion implantation. *Nano Energy* 90:106574. https://doi.org/10.1016/j.nanoen.2021.106574

7. Hasan M, Ety N, Islam F, Bhowmik S, Kamaruzzaman, Rana S (2026) Natural biowaste material-based green triboelectric nanogenerators for self-powered gait monitoring. *RSC Advances* 16(4):3281–3295. https://doi.org/10.1039/D5RA09038E
8. Hu Y, Tang C, Li S (2025) Flash annealing boosts piezoelectricity of PVDF-TrFE. *Nat Commun* 16:11147. https://doi.org/10.1038/s41467-025-67292-5
9. Inbaraj D, Gwak S, Lee J, Shin D (2026) Progress in PDMS modification strategies for high-performance triboelectric nanogenerators: design, applications and future perspective. *Current Opinion in Solid State and Materials Science* 43:101276. https://doi.org/10.1016/j.cossms.2026.101276
10. Ji M, Wang Z, Wang ZL (2025) Machine learning–assisted triboelectric nanogenerator technology for intelligent sports. *Science Advances* 11(40):adz3515. https://doi.org/10.1126/sciadv.adz3515
11. Jia N, He Q, Sun J, Xia G, Song R (2017) Crystallization behavior and electroactive properties of PVDF, P(VDF-TrFE) and their blend films. *Polymer Testing* 57:302–306. https://doi.org/10.1016/j.polymertesting.2016.12.003
12. Jiang H, Yang J, Xu F, Wang Q, Liu W, Chen Q, Wang C, Zhang X, Zhu G (2020) VDF-content-guided selection of piezoelectric P(VDF-TrFE) films in sensing and energy harvesting applications. *Energy Conversion and Management* 211:112771. https://doi.org/10.1016/j.enconman.2020.112771
13. Kumar D, Jin D, Jeong D, Kong D, Hu Y, Ko S, Lee K, Yoon S, Park J, Kim J, Jung J (2024) Boosted triboelectric output performance in g-C3N4 embedded P(VDF-TrFE) composite via a coupling of photocarrier and ferroelectric dipole. *Nano Energy* 122:109320. https://doi.org/10.1016/j.nanoen.2024.109320
14. Kumar D, Jin D, Hu Y, Ahn H, Jeon J, Ko S, Yoon S, Lee K, Kim J, Jung J (2025) Photoactive ferroelectric composite of g-C3N4@BaTiO3 in P(VDF-TrFE) polymer for enhanced triboelectric power generation. *Materials Today Energy* 53:101977. https://doi.org/10.1016/j.mtener.2025.101977
15. Lee C, Qin Y, Wang YC (2025) Triboelectric nanogenerators for self-powered sensors and other applications. *MRS Bulletin* 50(4):428–438. https://doi.org/10.1557/s43577-025-00877-z
16. Lee MH (2026) Leaf Biowaste-Based Triboelectric Nanogenerators for Clean, Affordable, and Sustainable Direct-Current Energy Harvesting. *Advanced Sustainable Systems* 10(6):e70542. https://doi.org/10.1002/adsu.70542
17. Li C, Yang X, Tang X (2025) High-Performance Triboelectric Nanogenerator Based on PVDF Nanofibers Modified by a Charge Control Agent n-Propyl Gallate. *Materials* 18(13):3089. https://doi.org/10.3390/ma18133089
18. Lin S, Guo Y, Wu C (2026) TENG-Based Self-Powered Silent Speech Recognition Interface: from Assistive Communication to Immersive AR/VR Interaction. *Nano-Micro Letters* 18(1):143. https://doi.org/10.1007/s40820-025-01982-z
19. Liu T, Chen D, Yang F, Chen J, Cao Y, Xiang M, Kang J, Xu R (2019) Enhancing the permeability and anti-fouling properties of a polyamide thin-film composite reverse osmosis membrane via surface grafting of l-lysine. *RSC Advances* 9(35):20044–20052. https://doi.org/10.1039/c9ra02773d

20. Liu Y, Wang F, Chen X, Cui F, Lu Y, Gao R (2026) Enhanced Output Performance of NaNbO3/P(VDF-TrFE)-Based Piezoelectric Nanogenerators by Femtosecond Laser Surface Modification for Bioenergy Harvesting and Human Motion Monitoring. *ACS Sustainable Chemistry & Engineering* 14(12):5971–5983. https://doi.org/10.1021/acssuschemeng.5c12562
21. Meng N, Ren X, Zhu X, Wu J, Yang B, Gao F, Zhang H, Liao Y, Bilotti E (2020) Multiscale understanding of electric polarization in poly (vinylidene fluoride)-based ferroelectric polymers. *Journal of Materials Chemistry C* 8(46):16436–16442. https://doi.org/10.1039/d0tc04310a
22. Montero K, Guzman R, Tewari A, Zou H, Wang ZL (2024) Printed and Stretchable Triboelectric Energy Harvester Based on P(VDF-TrFE) Porous Aerogel. *Advanced Functional Materials* 34(8):2312881. https://doi.org/10.1002/adfm.202312881
23. Nurmakanov Y, Kalimuldina G, Bakenov Z (2021) Structural and Chemical Modifications Towards High-Performance of Triboelectric Nanogenerators. *Nanoscale Research Letters* 16(1):122. https://doi.org/10.1186/s11671-021-03578-z
24. Rana S, Sharma H, Bokolia R, Bhatt K, Singh R, Meena R, Singh B (2025) PVDF/N-rGO nanofibers based sustainable triboelectric nanogenerator for self-powered wireless motion sensor. *Carbon* 234:119926. https://doi.org/10.1016/j.carbon.2024.119926
25. Saadatnia Z, Mosanenzadeh S, Esmailzadeh E (2019) A High Performance Triboelectric Nanogenerator Using Porous Polyimide Aerogel Film. *Scientific Reports* 9:1370. https://doi.org/10.1038/s41598-018-38121-1
26. Sharma A, Agarwal P (2024) Experimental study to analyse the effect of force-frequency mutual dependency on the performance of vertical contact-separation triboelectric energy harvester. *Journal of Vibration Engineering & Technologies* 12:4097–4107. https://doi.org/10.1007/s42417-023-01107-z
27. Shen W, Deng T, Shi J, Yang D, Nie Y, Zhang X, Xiang G (2026) A high-performance low-cost triboelectric nanogenerator enabled by biomass-derived carbon in PVDF nanofibers. *Nanoscale* 18(20):10736–10743. https://doi.org/10.1039/D6NR00092D
28. Troncoso OP, Corman-Hijar JI, Torres FG (2023) Lignocellulosic Biomass for the Fabrication of Triboelectric Nano-Generators (TENGs)—A Review. *International Journal of Molecular Sciences* 24(21):15784. https://doi.org/10.3390/ijms242115784
29. Wang Y, Zhu L, Du C (2021) Progress in Piezoelectric Nanogenerators Based on PVDF Composite Films. *Micromachines* 12(11):1278. https://doi.org/10.3390/mi12111278
30. Wibisono Y, Adriyanto M, Andriani M, Rizqi R, Shalahuddin I, Khotimah M (2025) Towards sustainable fabrication of modified PVDF membranes using CyreneTM: Exploring chitosan nanoparticles as bio-filler. *South African Journal of Chemical Engineering* 52:217–226. https://doi.org/10.1016/j.sajce.2025.01.012
31. Xiang H, Peng L, Yang Q (2024) Triboelectric nanogenerator for high-entropy energy, self-powered sensors, and popular education. *Science Advances* 10(48):eads2291. https://doi.org/10.1126/sciadv.ads2291

32. Yu S, Zhang Y, Yu Z, Zheng J, Wang Y, Zhou H (2021) PANI/PVDF-TrFE porous aerogel bulk piezoelectric and triboelectric hybrid nanogenerator based on in-situ doping and liquid nitrogen quenching. *Nano Energy* 80:105519. https://doi.org/10.1016/j.nanoen.2020.105519
33. Zhang J, Brown G, Fu J, James P, Mukandiwa L, Huang X, Yu C (2020) Nanobiopesticides: Silica nanoparticles with spiky surfaces enable dual adhesion and enhanced performance. *EcoMat* 2(4):e12028. https://doi.org/10.1002/eom2.12028
34. Zhang R, Örtegren J, Hummelgård M, et al (2018) Harvesting triboelectricity from the human body using non-electrode triboelectric nanogenerators. *Nano Energy* 45:298–303. https://doi.org/10.1016/j.nanoen.2017.12.053
35. Zhou L, Liu D, Wang J, Wang ZL (2020) Triboelectric nanogenerators: Fundamental physics and potential applications. *Friction* 8(3):481–506. https://doi.org/10.1007/s40544-020-0390-3

Figures

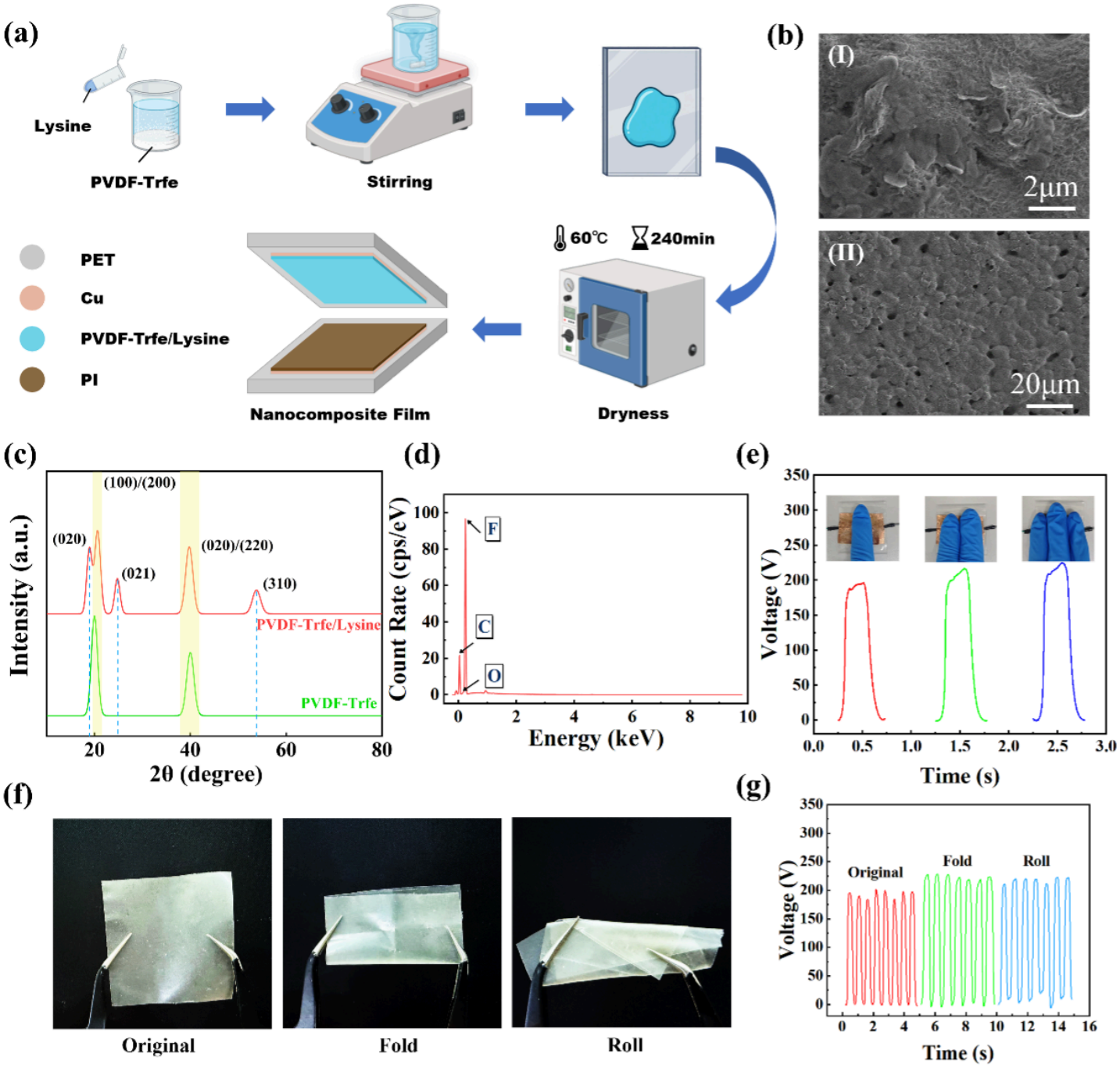


Figure 1

Structural design, material characterizations, and mechanical flexibility of L-lysine-modified PVDF-TrFE composite film-based TENG. **a** Schematic illustration of composite film preparation workflow. **b** SEM images of composite film surface morphology; scale bars: (I) 2 μm and (II) 20 μm. **c** XRD patterns of pristine PVDF-TrFE and L-lysine doped composite films. **d** Representative EDS spectrum of the doped composite film. **e** V_{oc} responses under finger pressing with varied contact areas. **f** Optical photographs demonstrating flat, folded, and rolled states of the composite film. **g** Comparative V_{oc} outputs for the device under flat, folded, and rolled mechanical deformation states.

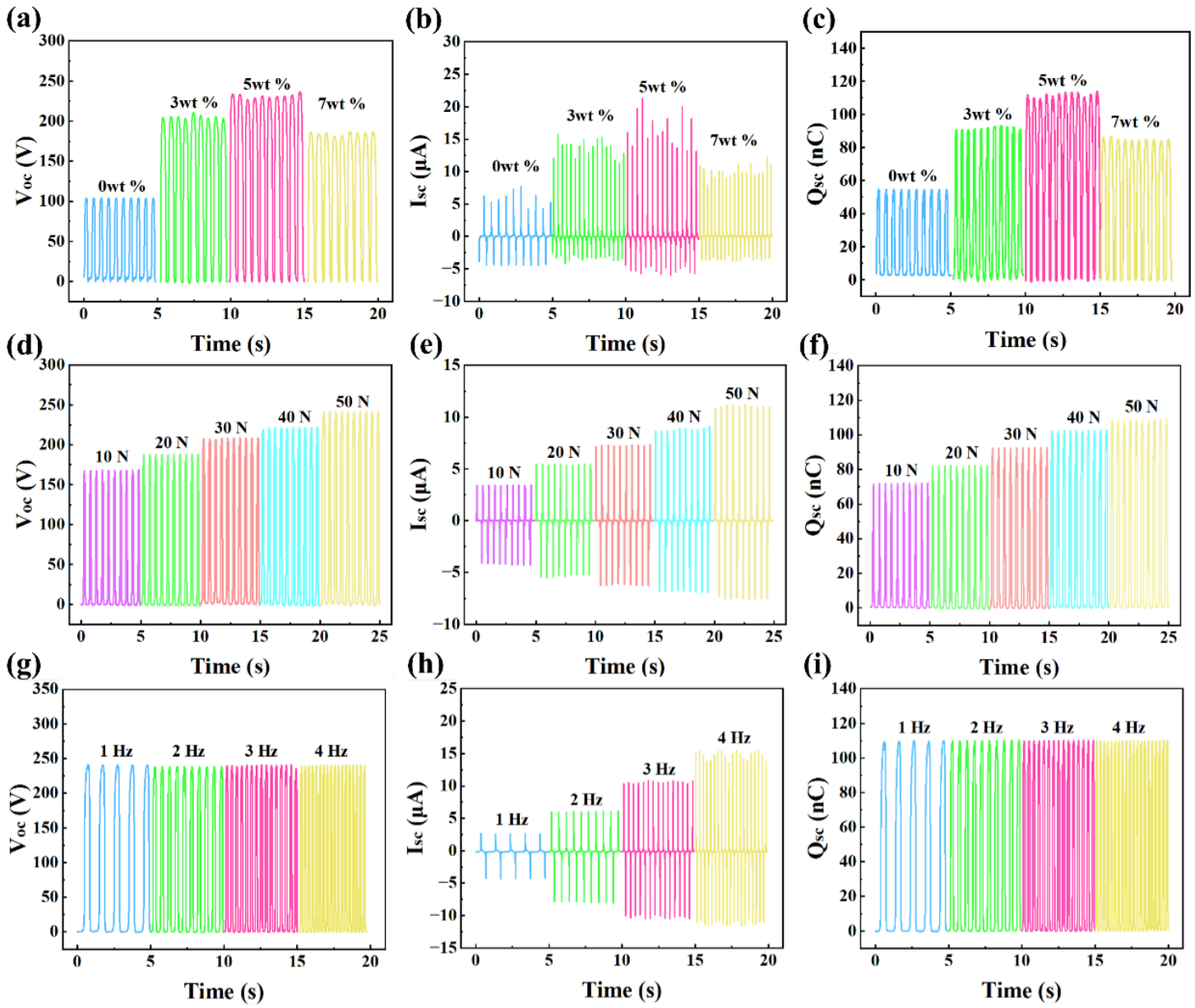


Figure 2

Electrical output performance of PL-TENGs as functions of L-lysine doping concentration, applied mechanical force, and operating frequency. **a-c** Open-circuit voltage, short-circuit current, and transferred charge of PL-TENGs with 0 wt%, 3 wt%, 5 wt%, 7 wt% L-lysine doping. The 5 wt% doped device delivers optimum output and was adopted for subsequent evaluations. **d-f** V_{oc}, I_{sc}, and Q_{sc} of optimized PL-TENG under varied applied forces (10-50 N). **g-i** V_{oc}, I_{sc}, and Q_{sc} of the optimized PL-TENG at different operating frequencies (1-4 Hz).

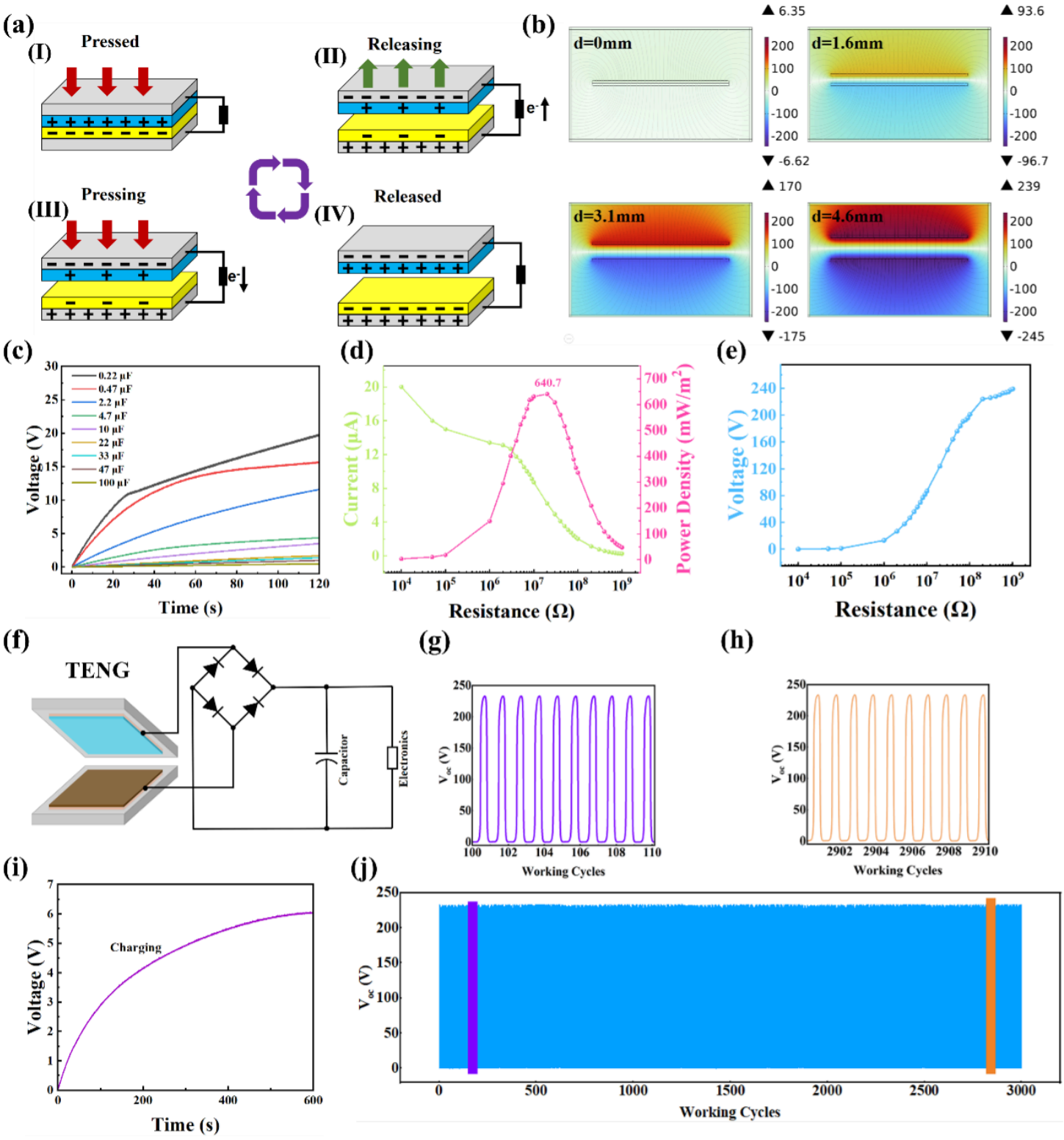


Figure 3

Device working principle, finite-element simulation, power output characterization, and cyclic durability of PL-TENG. **a** Schematic of four sequential stages within the contact-separation working cycle: (I) pressed, (II) releasing, (III) released, and (IV) pressing. **b** COMSOL-simulated electrostatic potential distribution at increasing separation gaps (d = 0 mm to 4.6 mm). **c** Capacitor-charging curves for different capacitance loads (0.22–100 μF). **d** Load-dependent current and power-density curves. **e** Output-voltage versus

external-load-resistance characteristic. **f** Circuit schematic incorporating rectifier bridge, energy-storage capacitor, and external load. **g** and **h** Magnified V_{oc} waveforms extracted from the initial and final segments of the cyclic durability test. **i** Charging curve for the storage capacitor powering a commercial thermo-hygrometer. **j** Long-term durability test over 3000 continuous contact-separation cycles.

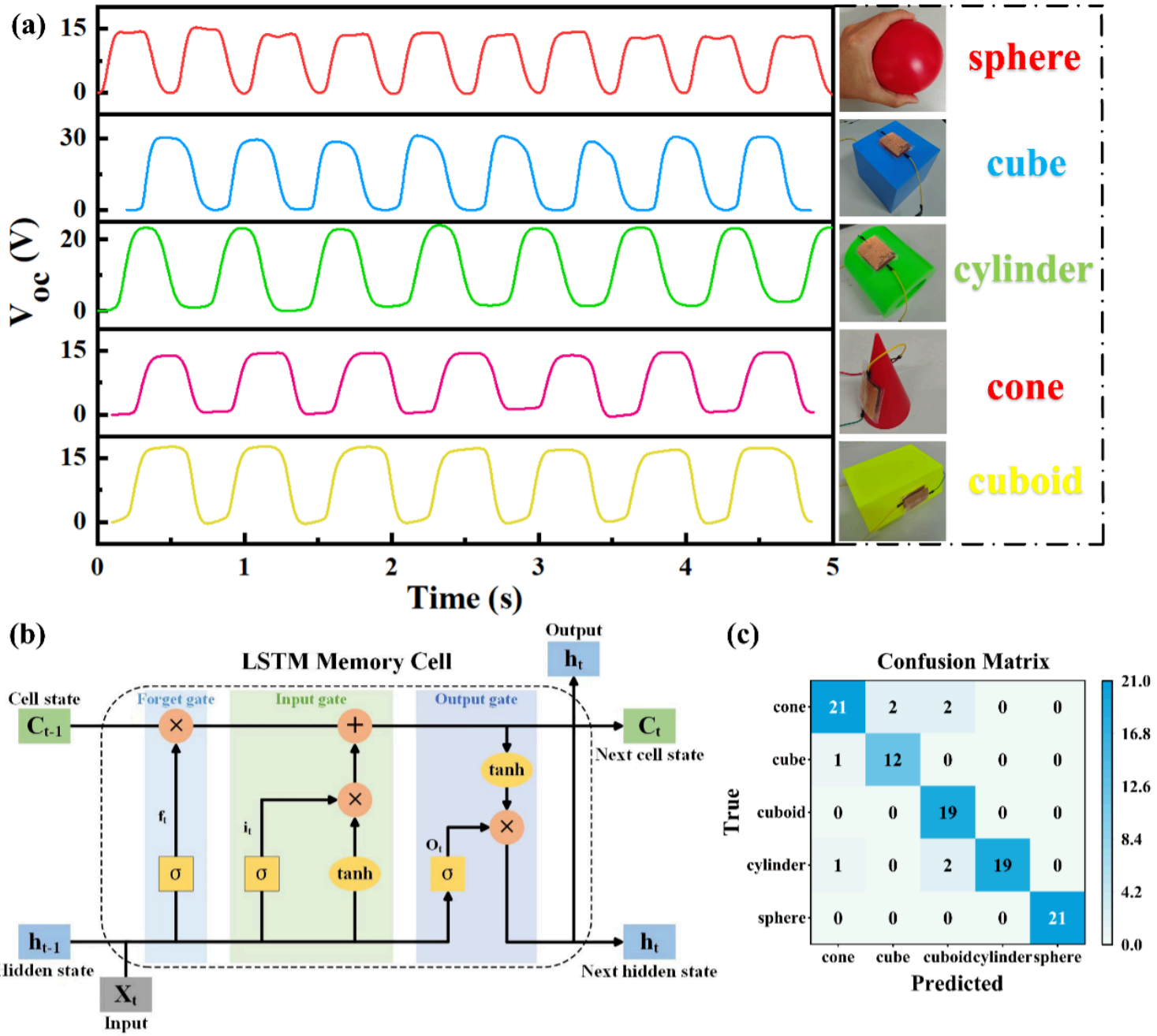


Figure 4

Deep-learning-enabled recognition of hand-gripped geometric objects using PL-TENG triboelectric waveforms. **a** Representative V_{oc} waveforms acquired when gripping five distinct geometric targets (sphere, cube, cylinder, cone, cuboid). **b** Architecture schematic of the CNN-LSTM hybrid deep-learning network, illustrating LSTM memory-cell internal gates. **c** Confusion matrix showing classification performance across five object categories.

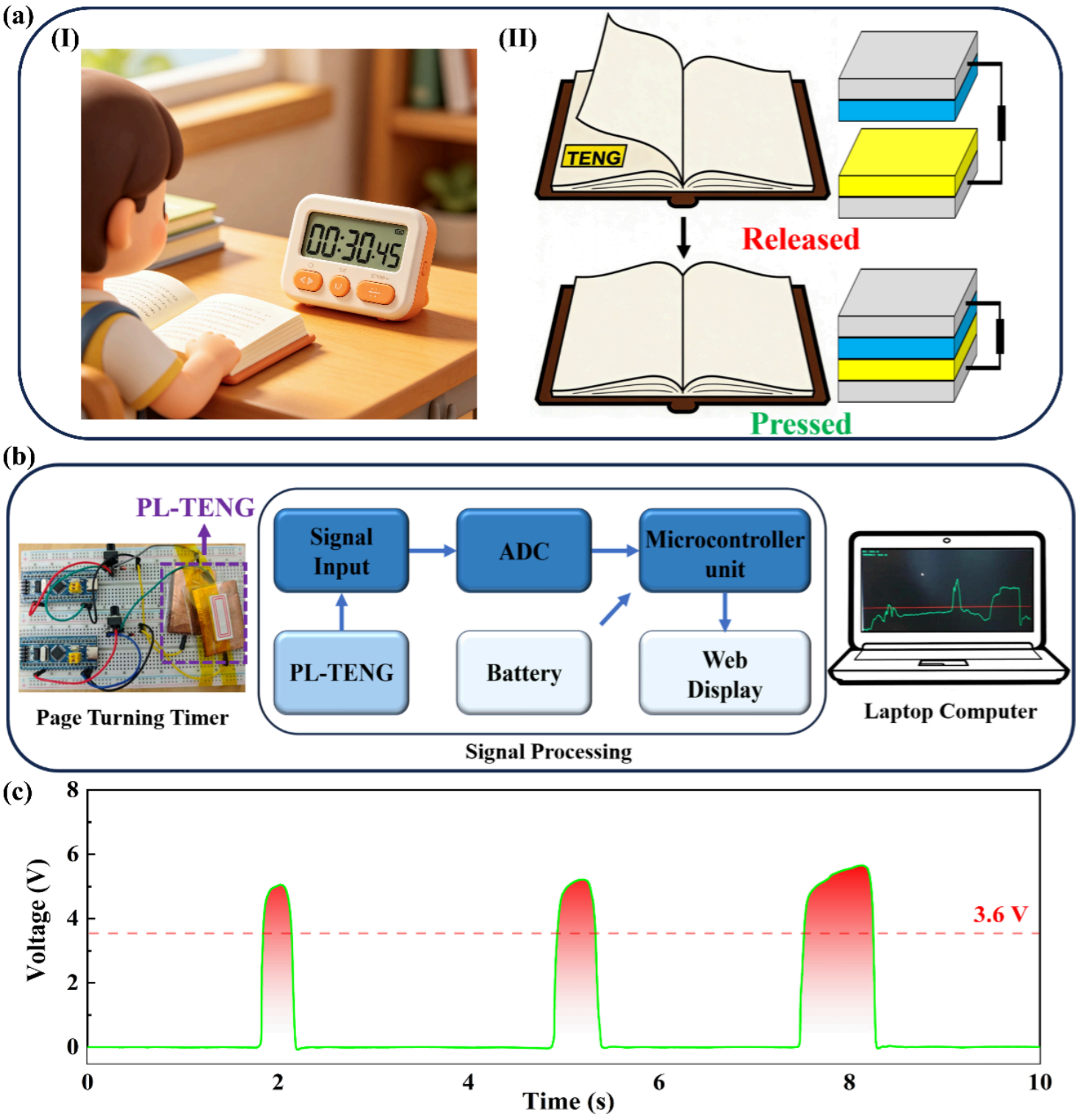


Figure 5

PL-TENG-based self-powered smart reading-timing system. **a** (I) Conceptual application scenario for desktop reading monitoring; (II) working principle: page-turning action triggers contact-separation of PL-TENG to generate sensing signals. **b**Photograph of hardware prototype and system-level functional block diagram (PL-TENG sensor, signal conditioning, ADC, MCU, battery, web-based visualization

terminal). **c** Real-time output-voltage waveforms recorded during page-turning events; preset trigger threshold = 3.6 V.

Supplementary Files

This is a list of supplementary files associated with this preprint. Click to download.

- Supportinginformation.docx
- SupportinginformationV1.mp4